



University
ofGlasgow

Experimental observations of droplet formation and polydispersity in T-junction microfluidic devices with pressure-driven flow

Aaron Delahanty
BSc Mechanical Engineering

School of Engineering
College of Science and Engineering
University of Glasgow

Submitted in fulfillment of the requirements for the Degree of
Master of Science

2016

Abstract

Microfluidic devices generally require precise control of fluid flowrates in order to reliably perform their various functions. Here a pressure-driven flow controller (PDFC) is developed and characterized for use as a flow provider for droplet-makers and as a tool for further microfluidics-based research.

The PDFC is first designed, manufactured and characterized prior to being applied to the study of droplet formation. Previously, droplet-makers that utilize volumetric flow control have been used to define the relationship between continuous and discontinuous phase flowrates and the resulting droplet parameters and flow regimes. Here, experimentation is conducted investigating the same droplet formation behavior but as observed in a system driven by pressure-based flow in a T-junction droplet generating device.

The PDFC system was characterized to show pressure control ranging from 0 to 1000mbar with 4 discreetly controlled channels capable of ± 1 mbar accuracy with a measured signal standard deviation of 0.25 mbar and signal to noise ratio of 400. The PDFC was then applied to microfluidic droplet production. Here, for the first time the transition from dripping to squeezing droplet formation regimes is clearly documented in a pressure-driven flow system. The resulting droplets show high monodispersity with less than 0.001 coefficient of variation in droplet length in all measured populations.

Contents

1	Introduction	1
2	System Development	2
2.1	Design	2
2.2	Characterization	8
3	Background Theory	11
3.1	Droplet microfluidics Overview	12
3.2	Determining System Flowrates	14
4	System Application - Droplet Microluidics	18
4.1	Aims	18
4.2	Methods	18
4.2.1	Device Generation	18
4.2.2	Experimental Procedure	19
4.3	Results	19
4.4	Discussion	24
5	Conclusions	31
A	Arduino Code	32
B	LabVIEW VI	36
C	Polydispersity Analysis	39
	Bibliography	42

List of Figures

2.1	Image of Packaged PDFC	4
2.2	Pneumatic Schematic of PDFC channel	5
2.3	LabVIEW write command	6
2.4	LabVIEW measured pressures	7
2.5	System Overview of the PDFC	7
2.6	PDFC time response	9
2.7	PDFC accuracy and inter-channel variation	10
3.1	System Scales	11
3.2	Hydraulic Resistance of System	16
4.1	Droplet Length as a Function of Applied Control Pressure Ratio . . .	19
4.2	Droplet length as a function of Capillary number across squeezing and dripping regimes	21
4.3	Polydispersity	22
4.4	Menech Regime Transition	24
4.5	Critical capillary number as a function of continuous phase applied pressure	25
4.6	Pressure Balance at no-flow condition.	26
4.7	Corrected capillary number as a function of continuous phase applied pressure	27
4.8	Droplet Velocity as a function of Applied Control Pressure Ratio . . .	28
4.9	Velocity, U as a function of applied pressure	29
4.10	Droplet Length as a Function of Applied Control Pressure Ratio . . .	30
B.1	LabVIEW Frontend	36
B.2	LabVIEW Backend True	37
B.3	LabVIEW Backend False	38
C.1	Polydispersity at CA = 0.014	40

C.2 Polydispersity at CA = 0.018	41
----------------------------------	----

Chapter 1

Introduction

The study of microfluidics requires by definition generation of fluid flow. In research and experimental settings syringe pumps are commonly used as flow providers[6]. They offer the advantage of being capable of directly controlling the rate of flow in units of volume per time. Furthermore, programmable syringe pumps have been developed that allow for modulation of flowrate as a function of time. An alternative to syringe pump systems is pressure-driven flow in which precision regulated compressed gas is used to pressurize fluid-filled reagent reservoirs, which in turn drives flow through small diameter tubing and subsequently any applicable microfluidic device. A custom developed pressure-driven flow system may offer advantages such as increased flow stability, capability to support high numbers of parallel flow channels, and ease of regulation. This project focus on the development of such a system, herein referred to as a Pressure Driven Flow Controller (PDFC).

The work documented here can be divided into two primary categories. First, the PDFC system is designed, built, and characterized. Secondly, the developed device is put to use to characterize micro-droplet formation in T-junction geometry operating under pressure-driven flow. The thesis presented herein is to be divided accordingly. First the design, development, and characterization of the flow device is presented. Followed by a presentation of the background theory necessary to discuss droplet formation. Experimental observations are presented and discussed. Finally, a conclusion is presented that describes the major accomplishments and courses of further investigation.

The custom developed microcontroller code, LabVIEW Virtual Interface (VI), and an operational user manual are included in the appendices, should further research be conducted using the system.

Chapter 2

System Development

2.1 Design

System design is covered here with the intent of allowing for future modification or reproduction of the flow system. Development of neither the labVIEW Virtual Interface (VI) nor microcontroller are covered in detail but are presented in the attached appendixes. The electronics skills required to build the system include analogue and digital electronics but are of basic undergraduate level and are not covered in any detail here.

Design Inputs High level design inputs were generated by discussion with the the research group of Thomas Franke and may be summarized as follows:

1. The flow system shall be controlled by a labVIEW VI.
2. The flow system shall feature four discrete pressure channels.
3. The flow system shall be capable of producing pressure output from 0 to 1 bar.
4. The resulting controlled pressure shall be visible to and recordable by the user.

System Components In order to develop a system capable of meeting these design inputs several key components are required, specified in Table 2.1

Component	Manufacturer	Part Number	Quantity
Regulators	Marsh Bellofram	Type 2000	4
Transducers	AMS	5915-1000-D	4
Transducers	AMS	5915-0350-D	4
DACs	MCP	4921	4
Microcontroller	Arduino	Uno R3	1

Table 2.1: Key System Components

Alternative components may be acceptable, even superior, to those detailed here. Specifically, pressure transducers that allow for faster modulation may be sought. The time response of the system developed here is covered in Section 2.2. In addition to the key components listed here other basic electrical components were required including standard off-the-shelf resistors, capacitors, molex-connectors and prototyping solderboard.

The system electronics are packaged within a IP 66/IP 67 DIN EN 60529 rated enclosure, shown in Figure 2.1 on the next page. The system functions as a 'black box' with the 240VAC – >9VDC power input, USB communication, main pneumatic supply line input, and 4 discrete regulated pressure outputs.

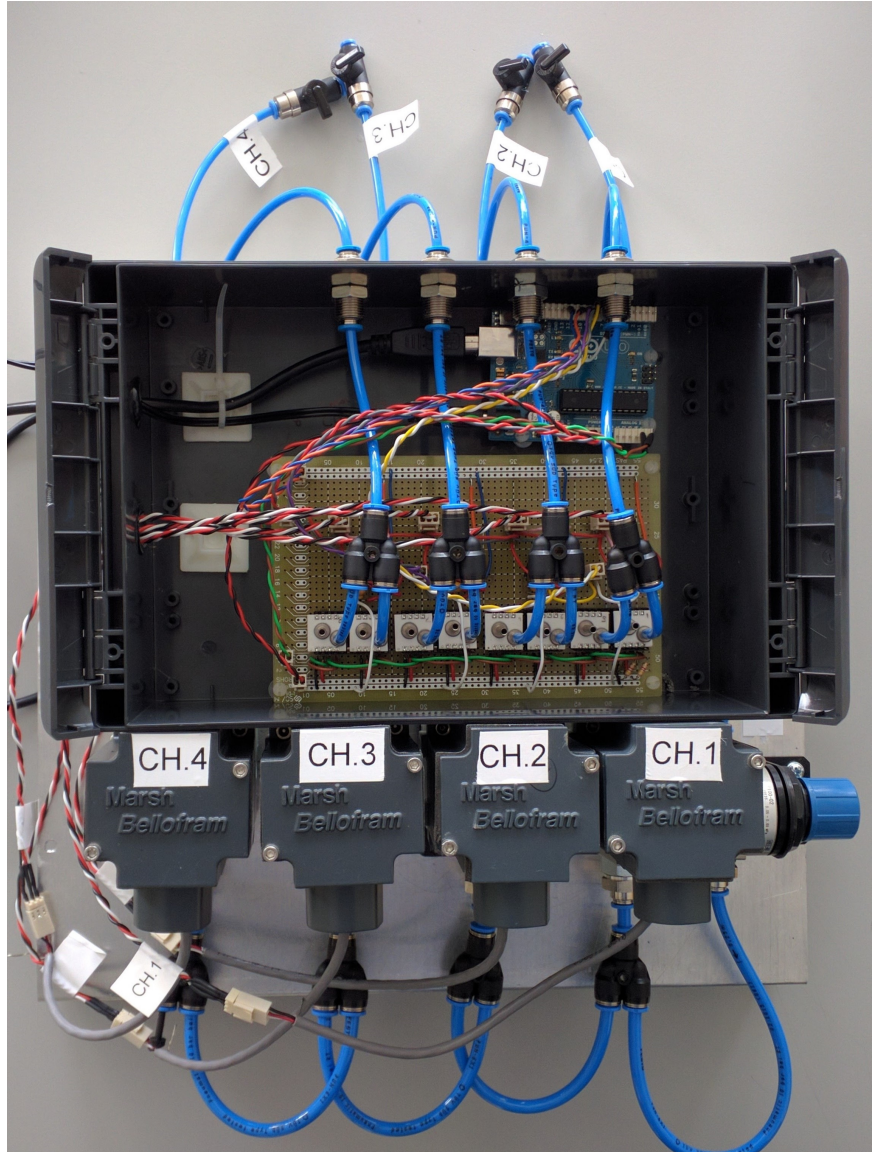


Figure 2.1: The PDFC as contained in the final enclosure.

Several pneumatic components are required to provide a compressed gas flow path between the supply, the regulators, transducers, and reagent reservoirs. These components are summarized in the pneumatic schematic for a single channel is shown in Figure 2.2 on the following page. Note that the air supply here is expected to be filtered to remove excess humidity and provide 3 micron particle filtration.

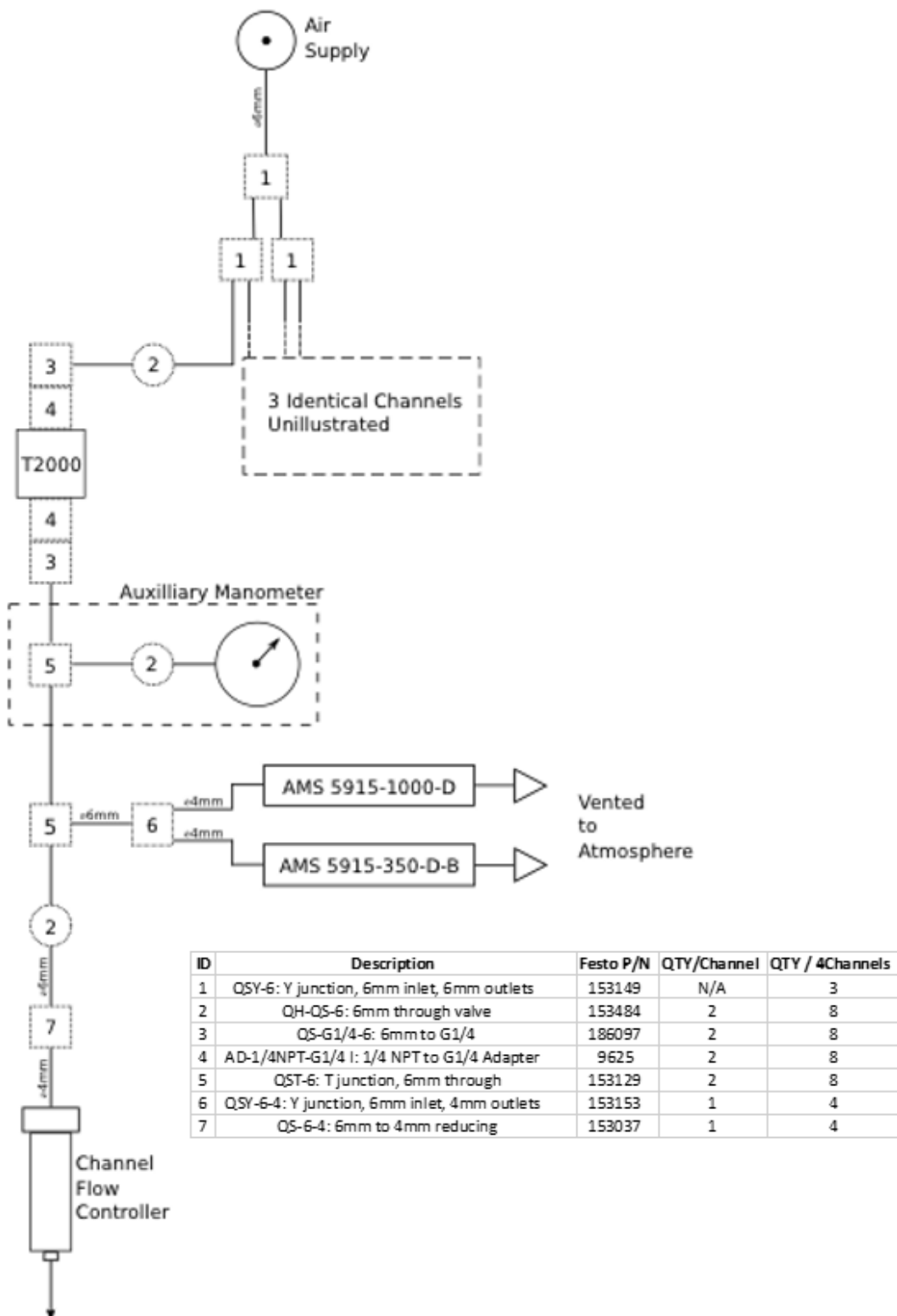


Figure 2.2: The pneumatic schematic detailing a single channel of the PDFC. The four primary components moving down through the schematic are the supply, T2000 pressure regulator, AMS pressure transducers, and the terminal flow reservoir.

Operational Overview The PDFC system is designed to be managed by interaction with a custom LabVIEW VI. The user manually enters a desired control signal within the labVIEW interface of 0 to 5 volts, corresponding to operational pressure range of 0 to 1000mbar.

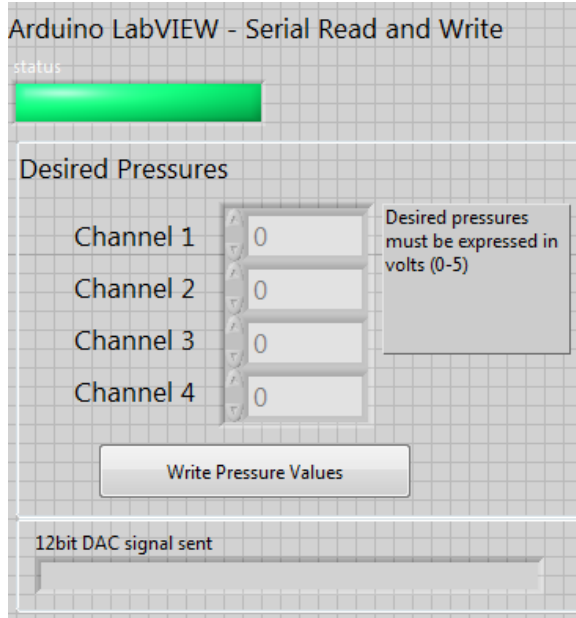


Figure 2.3: Control pressures are set digitally within the LabVIEW interface.

After initiating the write command the digital signal is written synchronously to the micro-controller by Universal Serial Bus (USB) via LabVIEW's 'virtual instrument software architecture'. The signal is initially sent and interpreted as a string and is processed via the embedded micro-controller code into a binary command comprised of the 4 configuration bits and 12 data bits. This binary command is then written to the digital analogue converters (DACs) via standard serial peripheral interface (SPI) protocol. The DACs convert the binary commands into analogue voltage outputs of 0-5V. This voltage is routed to the input of each pressure regulator and results in the desired pressure output of 0 to 1000 mbar.

The controlled output of each pressure regulator is then split by a y-connector. One flow path goes to the reagent reservoir to drive fluid flow, the other is routed back into the PDFC for real-time measurement by the integrated chip pressure transducers. Each regulated pressure channel is measured by two different 14bit transducers, one is low range (0-350mbar) with increased resolution, the other is full range (0-1000mbar). The pressure transducers produce a digital signal that is then transferred back to the

micro-controller via I2C protocol. Finally the measured pressures are sent to the LabVIEW VI for display and optional recording, shown in Figure 2.4.

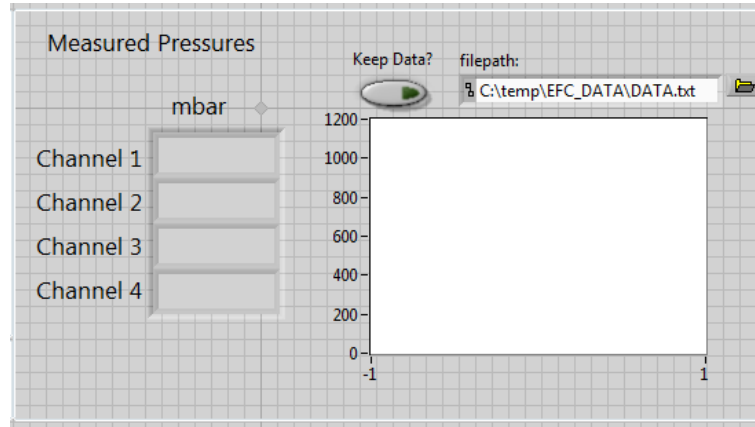


Figure 2.4: Measured pressures are presented as realtime values, and plotted in a virtual scope capable of being recorded.

This entire control process including LabVIEW and microfluidic device integration is summarized in system overview shown in Figure 2.5.

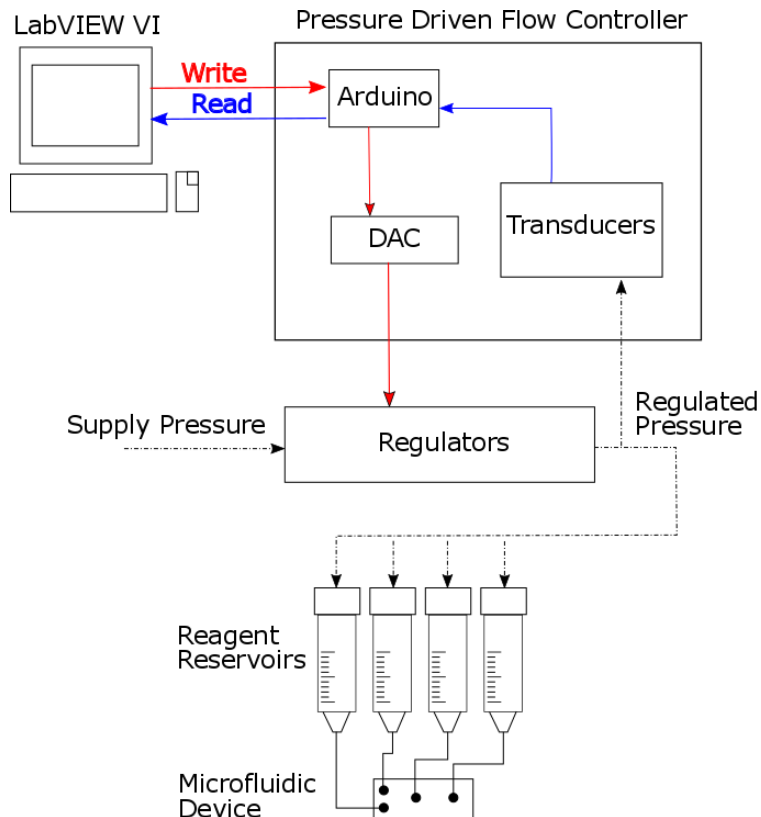


Figure 2.5: The control loop used to set and measure channel pressures using the PDFC

2.2 Characterization

After completing manufacture and integration of the PDFC it must be validated prior to being used as a research tool. Particular emphasis is placed on two operating criteria of the system:

1. The response time of the system, from application of write signal to regulated pressure response.
2. The accuracy and channel-to-channel variance observed in the system.

In regards to the response time of the system it may be valuable to detail the magnitude of individual response times for the process steps required from signal input to response output, summarized in Table 2.2

Process Step	Magnitude of Time Response(ms)
Sync. USB Comm.	1000
Arduino String -> Binary	1
DAC	1
Pressure Regulator	100

Table 2.2: Component Response Time

The labVIEW VI is capable of recording the measured regulated pressure outputs, which may be used to document control pressures employed for specific experimentation. Here, that data logging capability is used to investigate the system's time response, as shown in Figure 2.6 on the following page. The gap in data is due to use of 'synchronous' USB communication. The rightmost data prior to the gap coincides with the time point at which the command signal is sent. While all channel outputs clearly converge to the desired nominal output pressure, the time response is broadly speaking slow, and variation in channel regulation is apparent as the pressure output stabilizes. Variation in the stabilization of regulated signal is due to variance from regulator to regulator. The model of regulator used here relies on a Proportional Integral Differential (PID) control circuit with manually adjustable potentiometers to adjust gain constants, non-ideal when attempting to produce coincident outputs on discrete channels.

The time from signal write to that of reaching 95% of the desired output, τ , increases as a function of differential pressure sought but is roughly on the magnitude of 1sec.

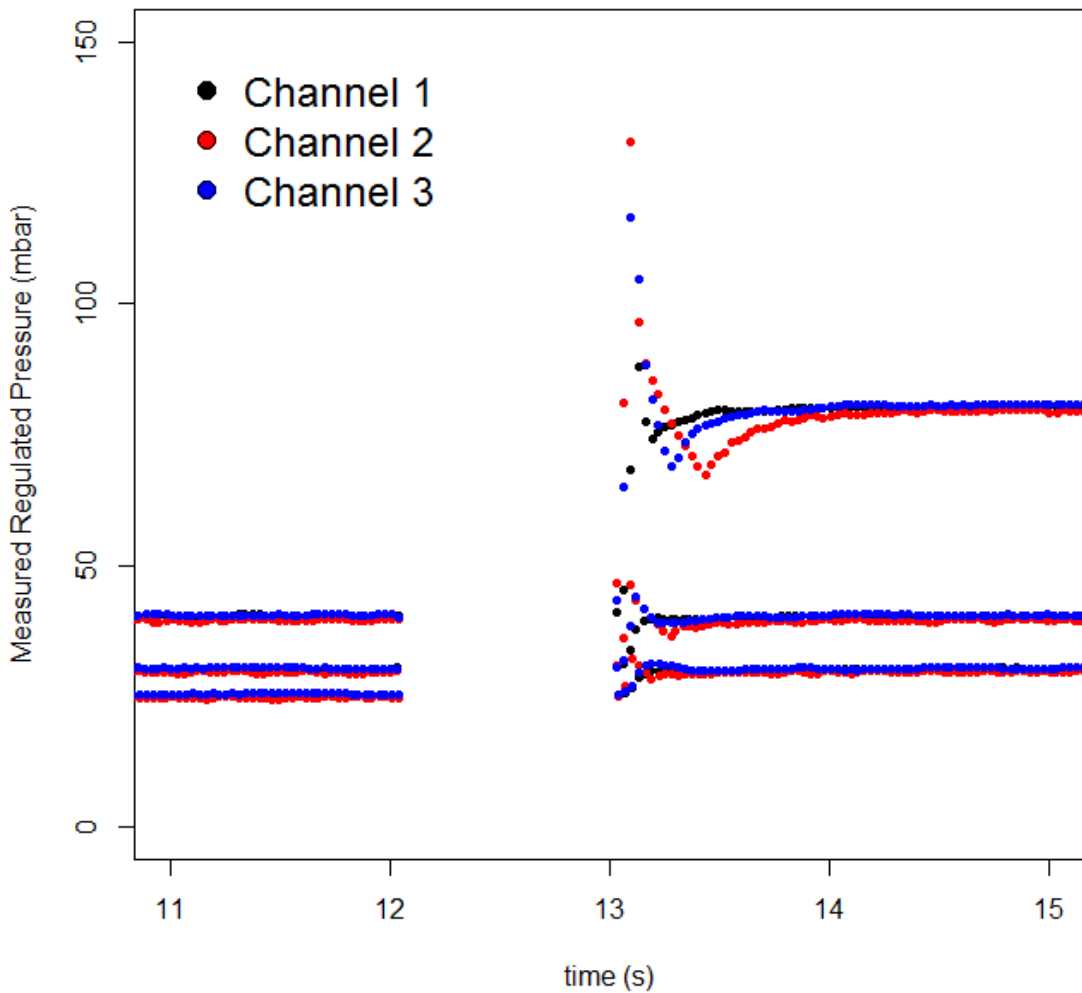


Figure 2.6: Three pressure transitions are shown, 40 to 80mbar, 30 to 40mbar, and 25 to 30mbar for 3 discrete output channels.

These observations suggests that the system as currently developed is not appropriate for the millisecond or faster response times required for real-time manipulation of droplet size. This agrees with previous findings. Flow rate control of droplet formation is known for its slow response whether by syringe pump or pressure flow. Furthermore, response time of the actual device is further delayed due to fluidic capacitance caused by the compressibility of reagents, tubing and PDMS channels [7, 16]. If fast-response times are sought a more appropriate methodology may be to maintain a steady flowrate and drive droplet formation by active methods through direct manipulation of the fluid at the local point of formation by electrical, mechanical,

magnetic, or acoustic means [5].

System accuracy and channel to channel variation can be investigated in a similar method to time response. Here, three channels are simultaneously regulated to a nominal 100mbar. After a stabilization time of approximately 3 seconds, a 15 second mean and standard deviation are acquired for each channel, as shown in area between the dashed lines in Figure 2.7. Each channel is capable of regulating to the nominal 100 ± 1 mbar with a standard deviation of less than 0.25 mbar.

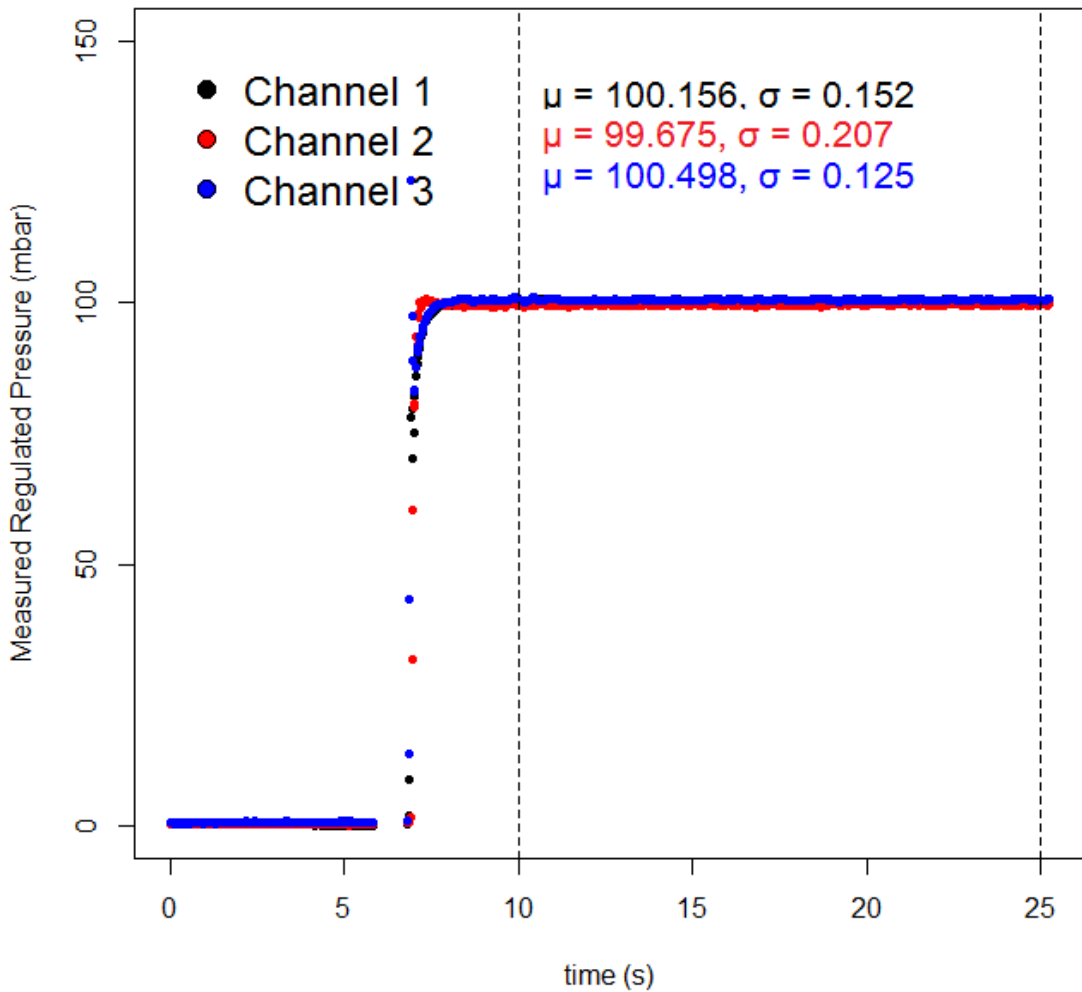


Figure 2.7: Accuracy and channel-to-channel variation of the PDFC system.

Chapter 3

Background Theory

Development of a pneumatic pressure driven flow system for use in microfluidic research requires a firm grasp on the transition from 'macro' fluidics to microfluidics. The system operates across a great range of scales drawing and compressing air from a room of several cubic meters that is subsequently used to provide flow in channels of only a few micrometers. Following the flow path of the system - compressed air is filtered and directed via large diameter (5mm) tubing to reagent columns of large diameter (2cm), where the compressed air acts on the reagent to produce flow through smaller tubing ($< 1\text{mm}$) before finally transitioning into the microfluidic device where channel dimensions are on the order of magnitude of micrometers.

The importance of forces that act on fluids therefore dramatically changes from the macro- to the microscale. With downscaling, the buoyancy, gravitational and inertial forces are less and less important and viscous and interfacial forces become more and more predominant.[15]

3.1 Droplet microfluidics Overview

Phase is a distinct state of matter in a system; matter that is identical in chemical composition and physical state and separated from other material by the phase boundary. Multiphase fluids are those in which there exist at least two different fluids in a system with different chemical compositions ? liquid/liquid, or with different physical states ? gas/ liquid.[15]. Here we neglect consideration of gas-liquid two phase systems.

[19, 14, 20]

The study of fluid dynamics requires the analysis of individual fluid forces (such as gravity, inertial, viscous, and interfacial forces) and an understanding of how these forces combine to define fluid behavior. In order to understand the transition from

large dimension ($> 1\text{mm}$) to small dimension ($< 1\text{mm}$) systems it may be useful to understand how these forces relate to system dimensions by the way of scaling laws. Some fluid forces such as inertial forces and gravity forces are dependent on the *volume* of fluid involved. Other fluid forces are intrinsically defined by the *surface area* of the fluids such as viscous forces and interfacial forces. More broadly speaking each of various fluid forces may be dependent on the different orders of characteristic length, l . For example, inertial force is dependent on density, ρ , which may be expressed as mass per volume or mass per l^3 , as shown in Equation 3.1 on the following page. Similarly, interfacial tension is often defined as the partial differential of the Gibb's free energy over area, where the area term may be expressed in terms of l^2 , shown in Equation 3.2.

$$i = \rho\nu^2 = \frac{m}{V}\nu^2 = \frac{m}{(l^3)}\nu^2 \quad (3.1)$$

$$\gamma = \frac{\partial G}{\partial A} = \frac{\partial G}{\partial(l^2)} \quad (3.2)$$

Consider the relative effect these individual forces have on the overall fluid behavior in which the volume dependent forces have an l^3 term and the surface forces have a l^2 term, as shown in Equation 3.3 on the following page [3]

$$\frac{\text{Surface Forces}}{\text{Volume Forces}} \propto \frac{l^2}{l^3} = l^{-1} \lim_{l \rightarrow 0} \rightarrow \infty \quad (3.3)$$

From this comes the realization that as systems are miniaturized towards a theoretical zero-dimension the surface forces begin play an exponentially larger effect relative to the volume forces.

Navier-Stokes Early attempts at approximating fluid flow by Bernoulli and his pupil Euler completely neglected the viscosity term (an aforementioned surface force) in their mathematical expressions. In systems of small dimensions the viscosity effects are dominant and these approximations are inadequate. The Navier-Stokes expression accommodates viscous forces and is essentially a statement of force balance between inertial, pressure and viscous forces, shown in Equation . In most microfluidic systems the inertial forces are small enough that they may be neglected and the expression reduces to the statement that the net pressure forces are equal to the negative net viscous forces [12].

$$\rho \left(\frac{\partial \nu}{\partial t} + \nu \cdot \nabla \nu \right) = -\nabla P + f + \eta \nabla^2 \nu + \nabla \sigma \quad (3.4)$$

$$\frac{\partial \nu}{\partial t} + \nabla \cdot (\rho \nu) = 0 \quad (3.5)$$

$$\rho \frac{\partial \nu}{\partial t} = -\nabla P + f + \eta \nabla^2 \nu + \nabla \sigma \quad (3.6)$$

above equations from [15]

Dimensionless Groups In many cases fluid flow at the microscale can be best categorized by comparing *dimensionless groups* driven by fluid parameters such as viscosity, velocity, density and system geometry, as is the case of the dimensionless group known as Reynold's Number (*Re*) shown in Equation 3.7 on the next page . Regardless of the specific fluid or geometric parameters, systems with similar *Re* numbers general behave similarly - making it powerful tool in characterization of a microfluidic system. The *Re* value can be described in real world terms as a relation between the inertial forces and viscosity forces at play in a system. At the microscale viscous forces are dominant over inertial forces thus the *Re* value is typically very low, indicating flow is laminar [10].

$$Re = \frac{\rho \nu L}{\mu} \quad (3.7)$$

Where ρ is fluid density, ν is fluid velocity, L is characteristic length, and μ is fluid viscosity. The *Re* value dictates whether the system will be within the laminar or turbulent regime. *Re* values tend to be small (< 1) for microfluidic systems because the spatial scales, and therefore characteristic length, are small while fluid viscosity is constant relative to larger-scale systems [4]. As the majority of microfluidic systems feature small *Re* numbers inertial forces are overwhelmed by interfacial forces in resulting in laminar flow and the dimensionless group becomes less valuable in the differentiation and categorization of different systems[15].

The Capillary number (*Ca*) is a dimensionless group that compares the relative contribution of interfacial forces and viscous forces. The capillary number is especially useful in discussion of two-phase microfluidic systems because it neglects any inertial forces and is capable of describing droplet formation behavior as influenced by solution viscosity and surface energies. The *Ca* is defined as shown in Equation 3.8 on the following page [4].

$$Ca = \frac{\mu u}{\gamma} \quad (3.8)$$

Where μ is defined as the viscosity of the continuous phase, u is the mean fluid velocity, and γ is the interfacial tension between the discontinuous and continuous phases. The viscous forces and interfacial forces determining fluid behavior are generally understood to act tangentially and normal to the two-phase interface, respectively. Viscous forces along the droplet surface work in elongation of surface of the droplet whereas interfacial forces work to minimize the interfacial area. These two opposing behaviors when acting in different ratios dictate the droplet behavior as categorized by the different fluid regimes dripping, squeezing, jetting(XX?)[15].

Two stable droplet formation regimes exist (i) *dripping* - in which the viscous forces associated with the continuous phase flow are significantly large to cause shearing of the immiscible thread and the production of a droplet prior to blocking the outlet channel and (ii) *squeezing* - in which the immiscible thread blocks the majority of the outlet channel prior to collapse and droplets are formed by a squeezing effect due to the pressure build up caused by the blocked channel.

3.2 Determining System Flowrates

One of the challenges in using pressure-driven flows for microfluidic research is the difficulty in determining local fluid velocities and flowrates within the microfluidic device. Several approaches are available to approximate the local device flow rates:

1. Experimentally: once the system is primed and running the waste reservoir can be weighed over some time interval, t , to determine the accumulation of fluid mass, M . Assuming the density of reagents is known, ρ , the mean flowrate, $Q(m^3 s^{-1})$, can be calculated as $Q = \frac{M}{\rho t}$.
2. Experimentally: while running, a visual indicator (such as beads, or droplets) can be measured by high speed camera to obtain an object velocity, V . Assuming the cross-section of the channel is known, A , the flowrate can be calculated as $Q = V \times A$.
3. Numerical Approximation: Assuming that all system dimensions and applied pressures are known, flowrates can be approximated by the analogous use of Ohm's Law, $\Delta V = IR$. Where voltage, V , current, I , and electrical resistance, R , are analogous to pressure, flow, and hydraulic resistance, respectively.

Hydraulic Resistance In order to numerically approximate the flowrate of microfluidic systems by use of hydraulic resistance a fundamental understanding of the Hagen-Poiseuille law is required. As previously stated, pressure, flowrate, and hydraulic resistance are analogous to Ohm's law as shown in Equation 3.9 on the next page [?].

$$\Delta p = R_{hyd}Q \quad (3.9)$$

The SI units of Hagan-Poiseuille are as shown in 3.10.

$$[Q] = \frac{m^3}{s} \quad [\Delta P] = Pa = \frac{kg}{ms^2} \quad [R_{hyd}] = \frac{kg}{m^4 s} \quad (3.10)$$

The hydraulic resistance varies based on specific channel geometry but the presence of a length to the fourth power is universal. This suggests that as channel dimensions increase the resistance decreases in a manner proportional to the dimensional change to the fourth power. This proportionality can be used to simplify the overall system considerably. Consider the simple generic system as shown in Figure 3.2 on the next page.

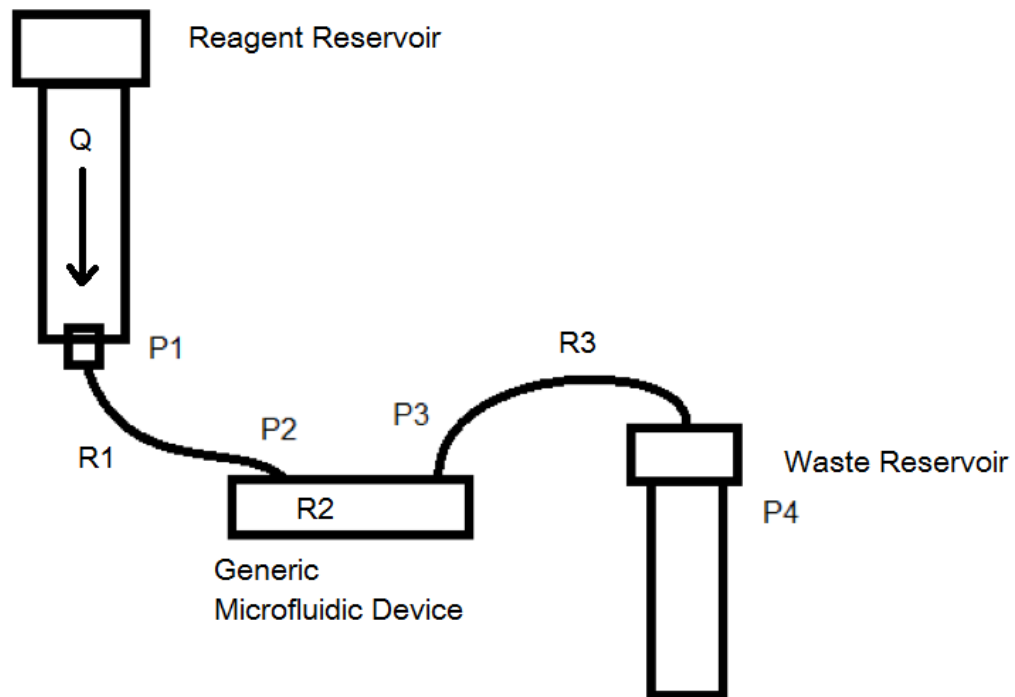


Figure 3.1: The microfluidic system detailed from the reagent water column to the waste reservoir.

The fluidic resistance present in the reagent reservoirs and tubing leading to the microfluidic device contribute to overall system resistance, and therefore flowrate. However, if the reservoir and tubing widths are substantially larger than the microfluidic device's channels the resistance and therefore contribution to system's pressure loss may be neglected.

For the purpose of quantifying the contribution to total pressure loss of tubing in a generic system the following arbitrary values are applied to first solve for the flowrate at an arbitrary applied pressure of 500mbar. Assume that P_4 is equivalent to atmospheric pressure, 0 Pa, and $L_1 = L_3 = 0.500\text{ m}$, $L_2 = 0.010\text{ m}$, viscosity $n = 1\text{ cP} = 0.001\text{ Pa s}$, tube radius $r = 0.00025\text{ m}$ and channel height $h = 0.00005\text{ m}$. Take $P_1 = 500\text{ mbar} = 50\text{ kPa}$ which is mid operational range for the system.

Consider the simple case shown in Figure 3.2 on the following page, and that hydraulic resistances in straight circular and square channels can be approximated as shown in Equations 3.11 and 3.12 on the following page, respectively.

$$R_1 = R_3 = \frac{8\eta L}{\pi r^4} = \frac{8(0.001)(0.500)}{\pi 0.00025^4} = 3.26 \times 10^7 \frac{\text{kg}}{\text{m}^4\text{s}} \quad (3.11)$$

$$R_2 = \frac{28.4\eta L}{h^4} = \frac{28.4(0.001)(0.010)}{0.00005^4} = 4.54 \times 10^{13} \frac{\text{kg}}{\text{m}^4\text{s}} \quad (3.12)$$

Clearly the resistance seen over the length of the simplified microfluidic device of dimensions $50\text{ }\mu\text{m} \times 50$ is several orders of magnitude greater than the resistance of the systems input and output tubing. If the total pressure ($P_4 - P_1$) is assumed to be an arbitrary value of 500mbar, flowrate can be calculated as shown in 3.13 on the next page.

$$P_4 - P_1 = (R_1 + R_2 + R_3)Q$$

$$Q = \frac{P_4 - P_1}{(R_1 + R_2 + R_3)}$$

$$Q = \frac{50,000}{(2(3.26 \times 10^7) + 4.54 \times 10^{13})} = 1.10 \times 10^{-9} \frac{\text{m}^3}{\text{s}} = 1.10 \times 10^{-6} \frac{\text{L}}{\text{s}} \quad (3.13)$$

Assuming that the system is at steady state and therefore the microfluidic structure (tubing and PDMS) is not expanding due to internal pressure we can infer that by conservation of mass and assumed incompressible fluids that the volumetric flowrate is constant across each of the system pressure points shown in Figure 3.2 on the

preceding page. Taking this constant flowrate and the previously found resistances individual pressure drops can be calculated as shown in Equation 3.14.

$$\begin{aligned} P_2 - P_1 &= (R_1)Q = 3.59 \times 10^{-2} Pa \\ P_3 - P_2 &= (R_2)Q = 4.99 \times 10^4 Pa \\ P_4 - P_3 &= (R_3)Q = 3.59 \times 10^{-2} Pa \end{aligned} \quad (3.14)$$

In this simplified case, representative of a typical microfluidic experimental set-up, the pressure loss due to the tubing as a percentage of the total pressure drop can be calculated as shown in Equation 3.15

$$\frac{P_3 - P_2}{P_4 - P_1} = \frac{3.59 \times 10^{-2}}{50.00 \times 10^3} = 7.18 \times 10^{-7} \quad (3.15)$$

And so it may be appropriate to neglect the pressure drops across the tubing and assume that the PDFC applied pressure is equivalent to the pressure applied across the microfluidic device. This can be further justified by the fact that the control precision of the system (shown to be 0.25mbar) is larger than the negligible pressure differentials of the tubing sections.

Chapter 4

System Application - Droplet Microluidics

4.1 Aims

The application of the PDFC to droplet microfluidics serves two purposes. First, it verifies that the system is functioning as intended for use as a research tool. Second, it allows the characterization of droplet formation by a pressure driven flow in conjunction with X and T-junction geometry, an area currently underdeveloped [6]. These aims can be fulfilled by the following two objectives:

1. Determine how applied pressure determine droplet formation regime
2. Relate applied pressure to droplet scaling law [20]

4.2 Methods

4.2.1 Device Generation

The T-junction microfluidic device referenced herein is fabricated using standard soft lithography methods [17]. Two part Polydimethylsiloxane (PDMS) was poured onto a SU-8 mold previously developed by Schmid and Franke [13] to form an array of individual T-junction channels. The PDMS was cured at 65dC for 3 hours. After cooling to room temperature, the set PDMS was cut and removed from the mold. Tubing connection holes were punched using a standard 0.5mm biopsy punch. Next, both glass slide and the PDMS are oxygen-plasma treated, adhered, and exposed to 100dC for 1hour. Prior to use, devices are treated with the aquapel for 10mins, purged with filtered compressed gas and dried at 65dC for 3 hours.

4.2.2 Experimental Procedure

Droplet formation was captured on a high speed camera at 2.5k to 20k frames per second. The applied control pressure was held constant for the continuous phase at a nominal value of 40, 60 and 80 mbar while varying the discontinuous phase control pressure. Discontinuous phase control pressure was varied at intervals of ≈ 5 mbar until droplet formation ceased due to the onset of backflow or instability, for low or high pressures, respectively. The captured images were then analyzed using a custom imageJ script to determine droplet length, L , and position, X , along an arbitrarily defined axis parallel to the geometry's outlet channel.

4.3 Results

For the T-junction channel geometry described the dimensionless droplet ratio of droplet length, L , over channel width, W , is plotted as a function of the applied control pressure ratios, $\frac{P_{H_2O}}{P_{Oil}}$, shown in Figure 4.1 on page 19. Error bars have been calculated by standard deviation of measured droplet length which results in error equal to or smaller than the symbol size and thus not shown.

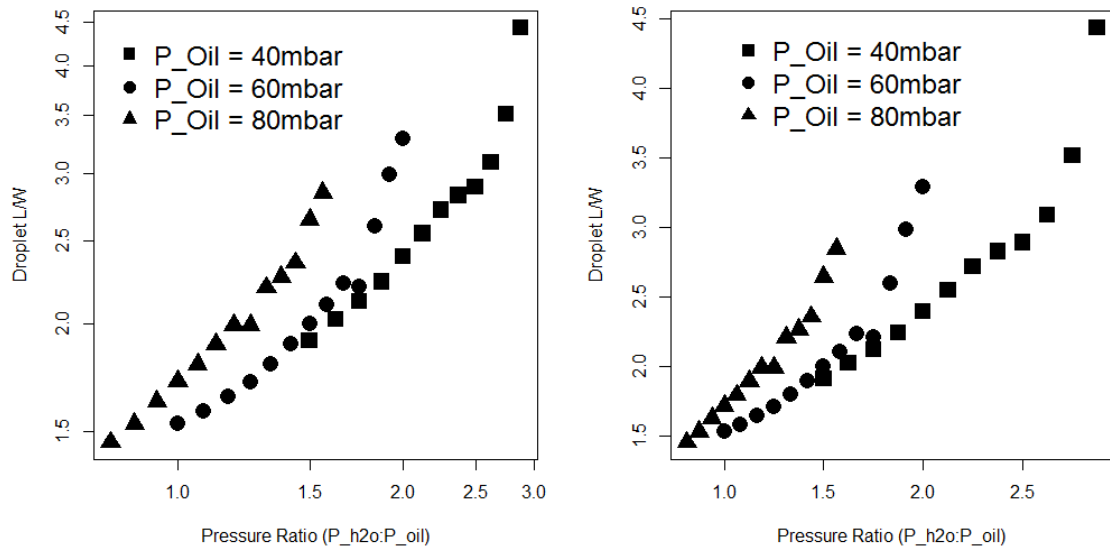


Figure 4.1: Log-log (left) and linear(right) plots of droplet length as a function of the applied control pressure ratio for T-junction geometry.

Outer Ca values are calculated given an interfacial tension of $\gamma = 2.87 \times 10^{-3} \frac{N}{m}$, continuous phase viscosity of $\mu = 1.24 \times 10^{-3} Pa \cdot s$ [1], and mean velocity, u , as

determined by droplet position over consecutive frames as shown in Equation 4.1 on the following page.

$$[u] = \left[\frac{\text{pixels}}{\text{frames}} \right] \left[\frac{\text{frames}}{\text{sec}} \right] \left[\frac{\text{meters}}{\text{pixel}} \right] = \left[\frac{\text{meters}}{\text{sec}} \right] \quad (4.1)$$

Droplet length is plotted as a function of capillary number as shown in Figure 4.2 on the next page for each of the applied continuous pressures. Images of droplet formation are shown within the squeezing and dripping regimes for each control pressure. The image shown was captured one frame prior to droplet formation.

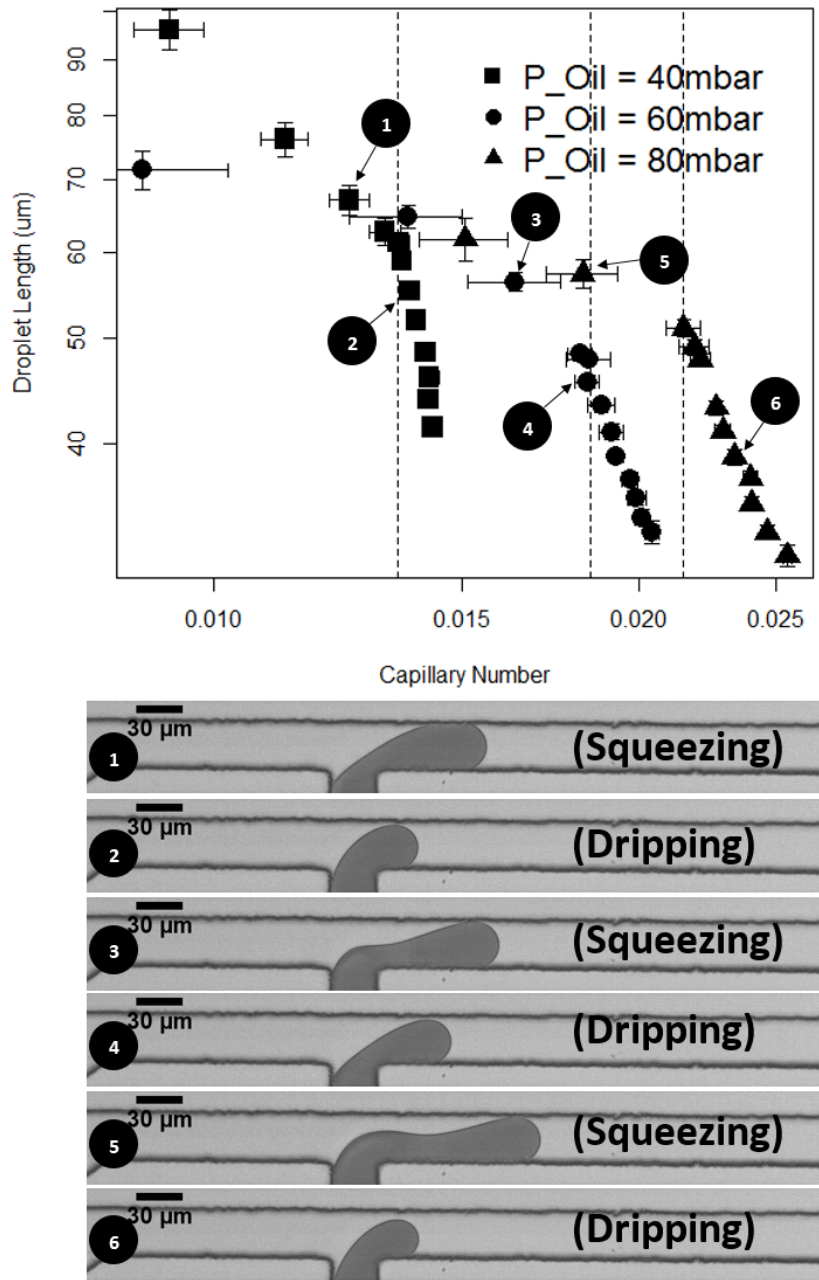


Figure 4.2: Top: Droplet length as a function of Capillary number across squeezing and dripping regimes, the transition between dripping and squeezing regimes is marked by vertical dashed lines. Bottom: Typical images of droplet elongation just prior to formation.

Variance in droplet dimensions is analyzed by evaluating the length of droplets formed by constant applied control pressures. Images were acquired at 500 fps for a period of 10 seconds resulting in a sample size of at least 100 droplets with at least three length measurements taken in subsequent frames per unique droplet. A

A variety of investigative plots are shown in Figure 4.3 on page 22, for data acquired at $P_{OIL} = 20\text{mbar}$, $P_{H_2O} = 80\text{mbar}$, resulting in a Ca value of 0.010. The same analysis was conducted at two higher Ca values and is found in Appendix Polydispersity.

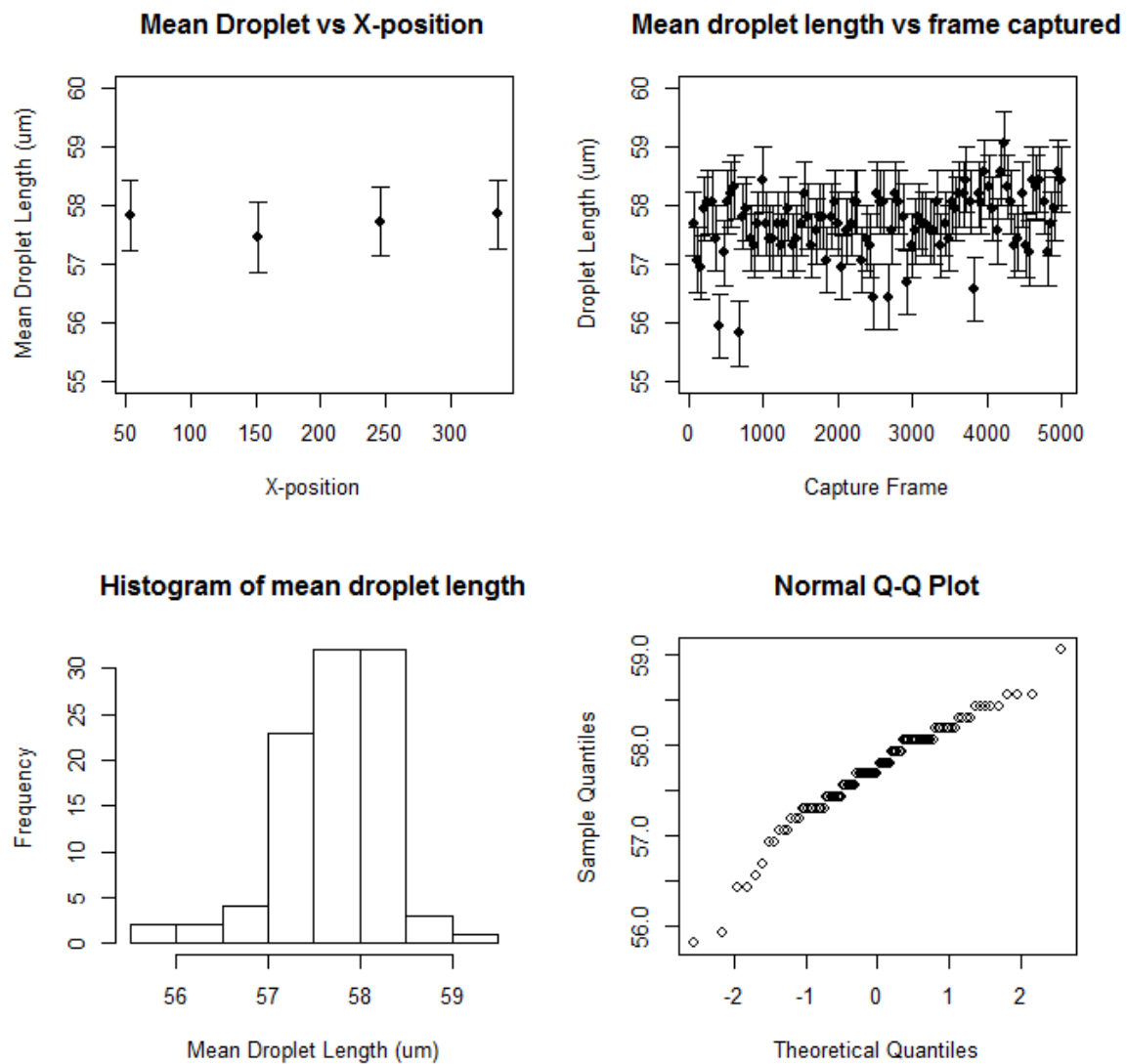


Figure 4.3: Distribution of droplet length for $P_{oil} = 0.1\text{bar}$

P_{Ratio}	Vel (m/s)	Ca	Mean Length(um)	StdDev(um)	Percent Var
4	0.023	0.010	57.71	0.55	0.95
2.25	0.033	0.014	54.53	0.35	0.64
1.66	0.043	0.018	48.14	0.21	0.43

Table 4.1: Dimensional analysis of droplets

From the analyzed data sets droplet velocity, capillary number, mean length, length standard deviation and percent variation ($lengthstdev/meanlength$) are extracted. A summary of the resulting dimensional statistics is shown in Table 4.1 on the next page.

4.4 Discussion

Previous work has been done to establish specific flow regimes in which droplets are formed in T-junction geometry by both numeric modeling and experimental investigations [2],[8],[9]. *However, to the best of the author's knowledge there has been no record of experimental observations demonstrating the regime transition from squeezing to dripping in a pressure-driven flow system.* This, despite the fact that there have been documented dissimilarities in volumetric versus pressure-driven flow in droplet formation[18], and that there may be advantages in droplet monodispersity in pressure-driven systems [6][11].

Previous findings suggest that two stable droplet formation regimes exist in T-junction droplet formation, *dripping* and *squeezing*. In a highly cited paper, De Menech et al showed by numerical modeling that the transition between the two distinct droplet regimes may be defined by a Critical Capillary Number, Ca_{cr} , and that this transition is independent of viscosity ratio and flowrates, shown in Figure 4.4 on the following page [8]. This transition has been previously determined both experimentally and in numerical simulations to be $Ca_{cr} \approx 10^{-2}$.

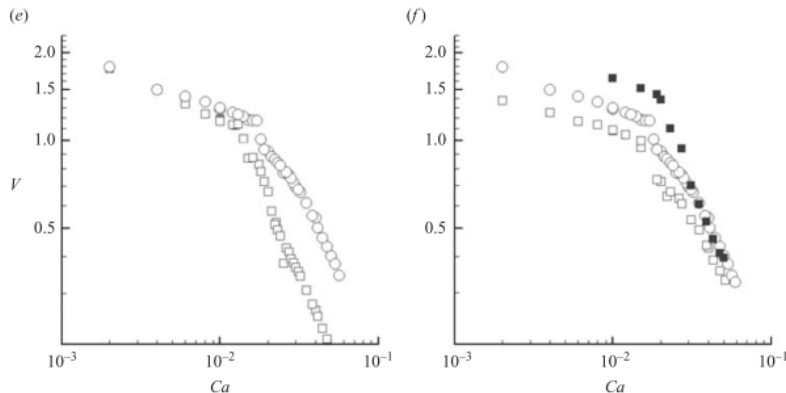


FIGURE 2. Drop formation as a function of capillary number. Two regimes of droplet formation are clearly distinguishable: at low Ca –(a) $Ca = 0.004, \lambda = 1$ – and high Ca –(b, c) $Ca = 0.035$ and $\lambda = 1/8$ and 1 respectively. At even higher Ca we observe the onset of a jet –(d) $Ca = 0.05, \lambda = 1$. (e, f) Log-log plot of droplet volume versus capillary number. (e) $Q = 1/4$, and $\square, \lambda = 1; \circ, 1/8; \diamond, 1/4$; (f) $\lambda = 1/8; \square, Q = 1/8; \circ, 1/4; \blacksquare, 1/2$. At high Ca , the droplet volume decreases more steeply, and is strongly influenced by the viscosity ratio λ .

Figure 4.4: Used directly, without permission

The data presented here shows a distinct transition between dripping and squeezing regimes, however, the Ca_{cr} value at which the transition occurs is not universal between the different continuous phase pressures. The transitional capillary number

can be plotted as a function of the continuous phase pressure as shown in Figure 4.5 on the next page.

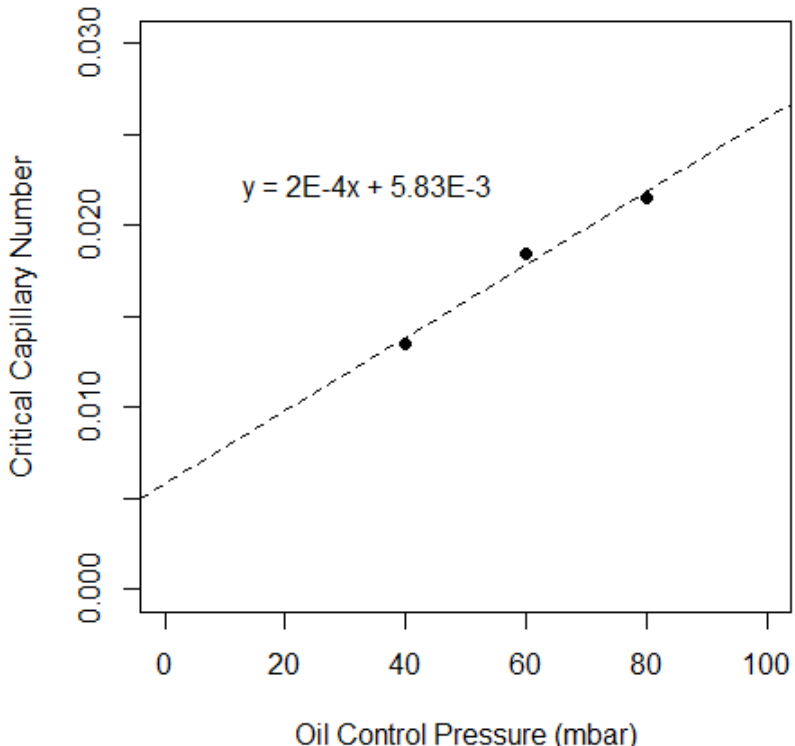


Figure 4.5: Critical capillary number as a function of continuous phase applied pressure

In these experiments the same bulk reagents are used and therefore both interfacial tension and viscosities should remain constant across multiple trials. Here, the only variable affecting variability in the Ca value is the mean velocity of the continuous phase, which in this case is approximated by direct measurement of the droplet velocity. It is expected that there is some numerical difference between the velocity of the droplets and the mean velocity of the continuous phase [18], which may account for the variability in critical capillary number.

Unfortunately due to the complex nature of multiphase flow during droplet formation it may be difficult to further investigate the true mean velocity of the continuous phase. However, there is one simplified case that allows for continuous phase flowrate and

therefore velocity approximation. That is the case at which no-flow occurs, immediately prior to initial droplet formation within the dripping regime. In this case force balance occurs such that the local continuous phase pressure is equal to the sum of the Laplace pressure and the local discontinuous phase pressure, shown in equation...XX.

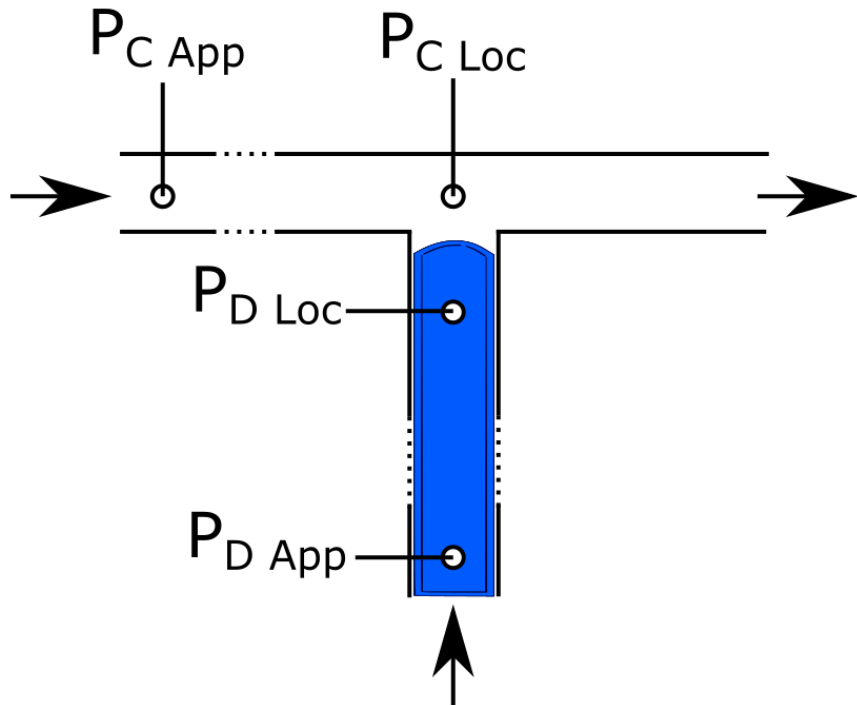


Figure 4.6: Pressure balance at no-flow condition

A model of Poiseuille flow in a rectangular channel could be used to provide a more accurate determination of the mean continuous phase velocity (as a function of droplet velocity. Alternatively, due to the linear nature of relationship between applied control pressure of the continuous phase and the critical capillary number the velocities could be corrected such that the regime transition is coincident, as shown in Figure 4.7 on page 27.

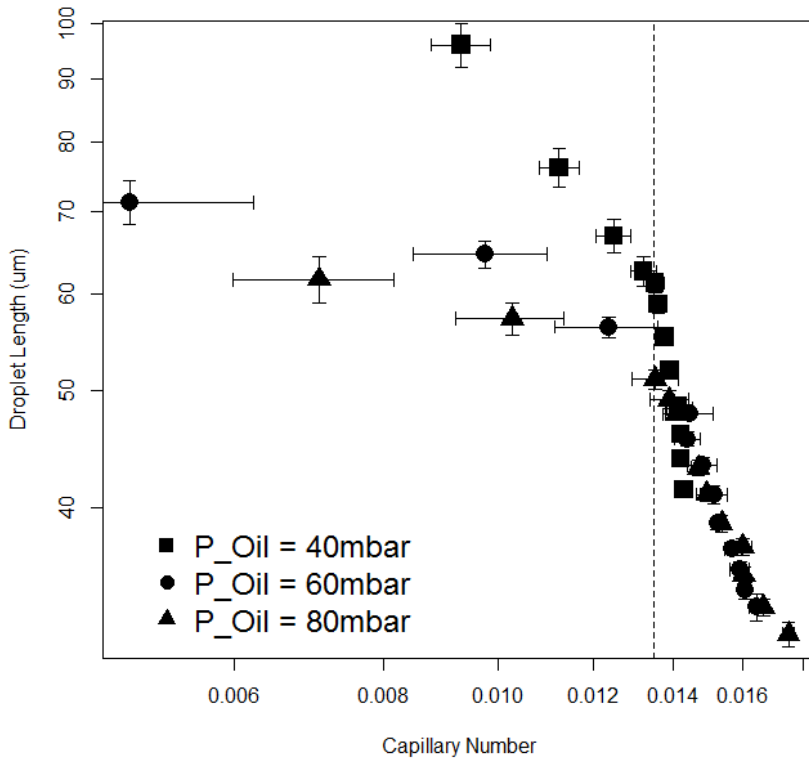


Figure 4.7: Corrected capillary number as a function of continuous phase applied pressure

In the system developed here, the only inputs used to manipulate flow behavior are the two applied pressures. Therefore, in order to characterize the system's flow regimes it is logical to determine the relationship between applied pressures and the resulting droplet velocity. Here, velocity is plotted as a function of the applied pressure ratio for both T and X-junctions as shown in Figure 4.8 on page 28. Ward determined the relationship for their system as shown in Figure 4.9 on page 29. (XX we need to do the same)

In order to qualitatively characterize the formation of droplets across the entire range of functional pressure ratios, the following section will describe the system behavior at the states of no-flow, dripping, squeezing, and onset of instability.

No-Flow As the system is moved towards the lowest operational pressure ratios, the aqueous phase comes to a quasi equilibrium no-flow state. As previously reported by Ward et al citeWard2005 . If the pressure ratio is decreased any further(either by increasing P_{Oil} or decreasing P_{H_2O}) back-flow will occur, in which the continuous

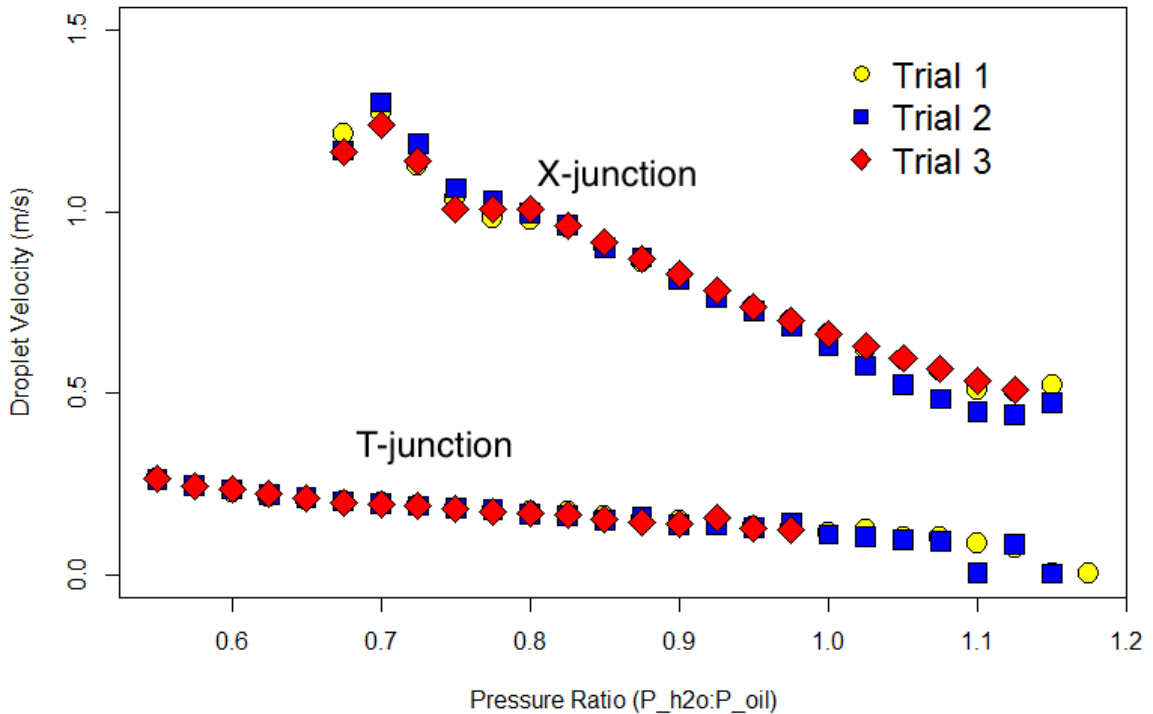


Figure 4.8: Droplet velocity for both T and X-junctions

phase begins displacing the aqueous phase upstream towards the reservoir. This quasi equilibrium state may be described as a balance of forces between the pressure of the two phases and the Laplace pressure differential across the liquid-liquid interface, described as shown in Equation 4.2 on the next page.

$$P_{H_2O*} + P_{Laplace} = P_{Oil*} \quad (4.2)$$

Where Laplace pressure can be roughly approximated given γ is the interfacial tension between the two phases, r is the radius of curvature of the interface as:

$$P_{Laplace} = \frac{2\gamma}{r} \quad (4.3)$$

It should be noted that here P_{H_2O*} and P_{Oil*} represent the pressures of the two phases local to the X or T junction and that there is some unknown pressure drop between the applied control pressures at the inlet reservoirs and these local pressures. This pressure drop is dependent on device geometry as well as solution viscosity and can be determined by Hagan-Poiseuille approximations (XX - needs to be done).

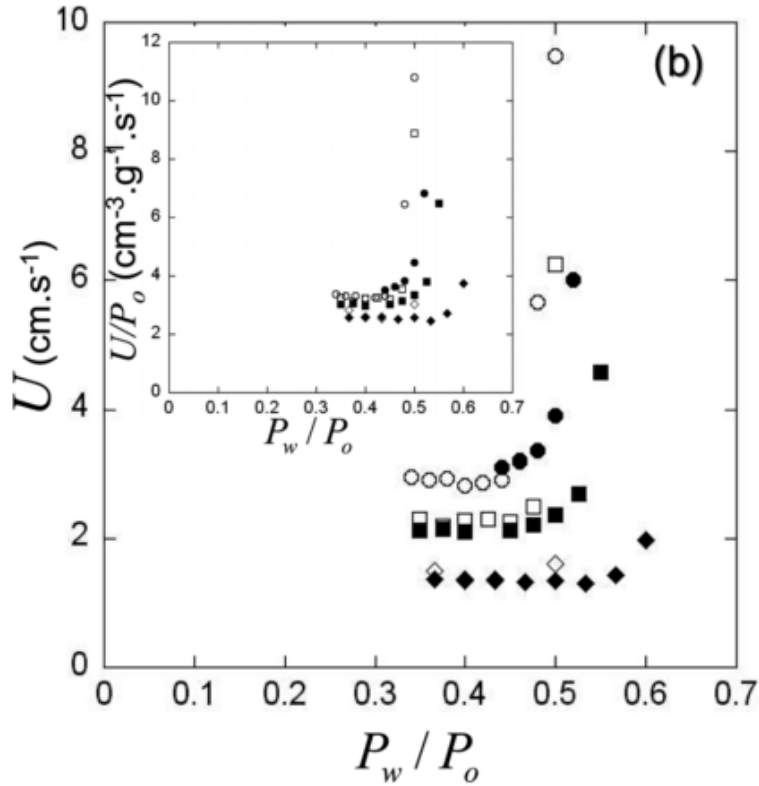


Figure 3. Measured velocity U versus (a) flow-rate where $\circ, \bullet Q_o = 2000 \mu\text{L}/\text{h}$, $\square, \blacksquare Q_o = 1000 \mu\text{L}/\text{h}$ and $(\diamond, \blacklozenge Q_o = 500 \mu\text{L}/\text{h}$ and (b) inlet pressure ratio where $\circ, \bullet P_o = 12.5 \text{ Psi}$, $\square, \blacksquare P_o = 10 \text{ Psi}$ and $\diamond, \blacklozenge P_o = 7.5 \text{ Psi}$. The open and closed symbols are for experiments where the dispersed phase fluid flow parameter is either increased or decreased respectively.

Figure 4.9: Used without permission, taken directly from [18]

Dripping As the control pressure applied to the discontinuous phase is increased beyond the *no-flow* state the immiscible thread begins to extend into the device's channel junction.

Squeezing The pinch point moving further downstream is a manifestation of the increases in tangential viscous forces relative to inertial forces (Ca). The Ca value increases due to the increase in velocity as the interfacial tension and viscosity are both constant. The viscous forces acting tangentially to the discontinuous phase boundary elongates the immiscible thread before the combined effect of increased plugging pressure and inertial forces finally dominate leading to droplet formation.

Outer Ca values are calculated at the transition between flow regimes given an interfacial tension of $\gamma = 2.87 \times 10^{-3} \frac{\text{N}}{\text{m}}$, continuous phase viscosity of $\mu = 1.24 \times$

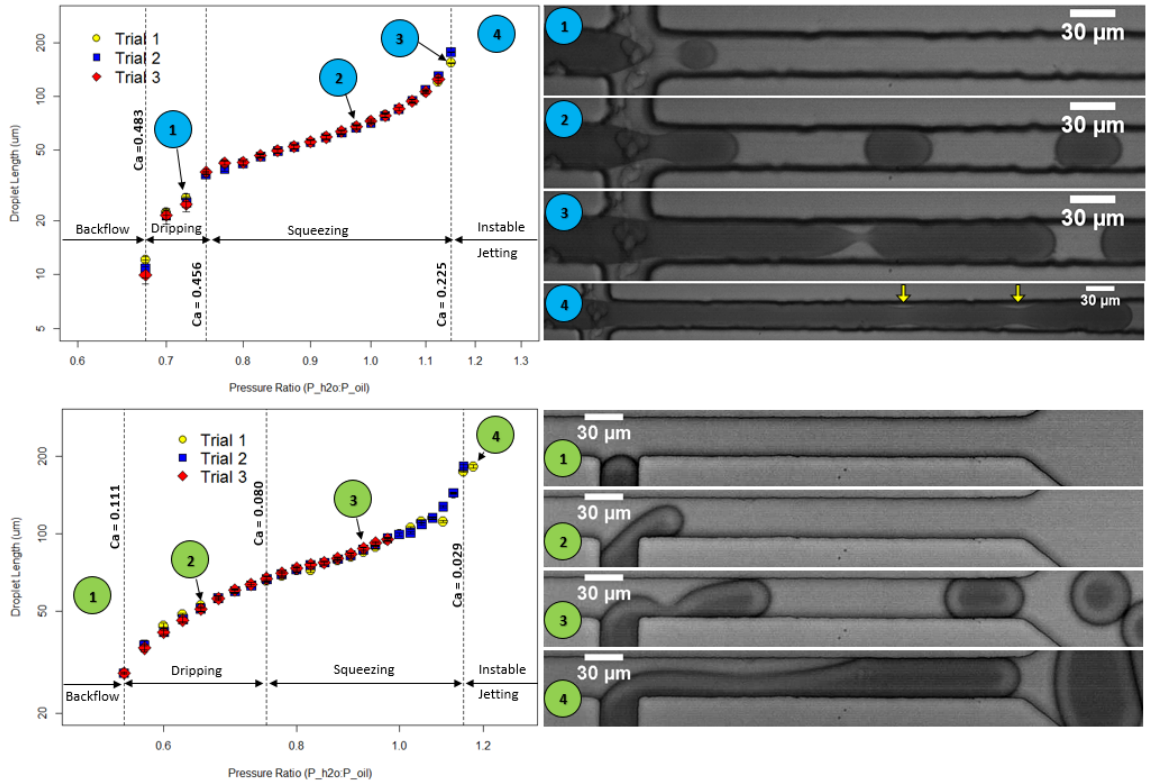


Figure 4.10: Log-Log plots of droplet length as a function of the applied control pressure ratio for X-junction (top) and T-junction (bottom) geometry. Select images are shown for each geometry showing the case of quasi-equilibrium (bottom-1), droplet formation within the dripping regime (top-1, bottom-2), droplet formation within the squeezing regime (top-2, bottom-3), migration of the 'pinch-point' along the longitudinal axis (top-3, bottom-4), and onset of jetting (top-4).

$10^{-3} Pa \cdot s$, and mean velocities, u , as determined by droplet x-position.

Chapter 5

Conclusions

Appendix A

Arduino Code

```
//Aaron Delahanty
//2224135D@student.gla.ac.uk
//University of Glasgow
//21Oct2015
//Electronic Flow Controller

//This application (sketch) is intended to be the sole sketch responsible for
//measuring
//and regulating pressure in the Electronic Flow Control (EFC) system being developed
//for T.Franke's microfluidic group. The objective of the sketch is to facilitate
//communication with two types of integrated chips (i) Analog Microselectronic's
//AMS5915
//pressure sensors, and (ii) Microchip Technology Inc.'s MCP4921 DAC.

//In addition to this sketch the system will use a LabView VI to set the desired
//pressure values by DAC, and display the measured pressure for the 4 discrete
//channels
//This communication will be facilitated by serial communication over USB.

//Revision Notes:
//02192016 - Removed Voltmeter functionality
//           - Removed All Delays
//           - 4th Channel DAC is faulting (output is always 1V)

//Wire.h is the arduino library for I2C/TWI comm
#include <Wire.h>
#include <SPI.h>

//Define variables used for conversion of pressure units from raw counts mbar.
int p_min;
int p_max;
int digoutp_min;
int digoutp_max;

//Define array for pressure channel comparison and final output
//Comparison is used to determine whether the high range 1000mbar or high resolution
//350mbar sensor should be used
float p_comp[8];
float p_out[4];

//Prior to sending the 12bit input which will drive the T2000 pressure regulators
//the DAC needs to receive 4 configuration bits
//Bit 15 - 0 = write to DAC, 1 = ignore command
//Bit 14 - BUF; 1 = buffer v_ref, 0 = bypass buffer
//Bit 13 - GA; 1 = v_out is 1X v_ref, 0 = vout is 2X v_ref
```

```

//Bit 12 - SHDN; 1 = active, 0 = shutdown DAC

//Default configuration bits set to [0,1,1,1]
unsigned int Config = B0111;

void setup()
{
    //Set baud rate to 9600
    Serial.begin(9600);
    // join i2c bus
    Wire.begin();
    // join SPI bus
    SPI.begin();
}

void loop()
{

//START DAC CODE:

// check serial

if ( Serial.available() ){
    // cast the string read in an integer
    String p_write = Serial.readString();

    int commaIndex1 = p_write.indexOf(',');
    int commaIndex2 = p_write.indexOf(',',commaIndex1+1);
    int commaIndex3 = p_write.indexOf(',',commaIndex2+1);

    String P1s = p_write.substring(0,commaIndex1);
    String P2s = p_write.substring(commaIndex1+1,commaIndex2);
    String P3s = p_write.substring(commaIndex2+1,commaIndex3);
    String P4s = p_write.substring(commaIndex3+1);

    unsigned int a[3];
    a[0]=P1s.toInt();
    a[1]=P2s.toInt();
    a[2]=P3s.toInt();
    a[3]=P4s.toInt();

    float cs[3];
    for (int i = 0; i <= 3; i++)
    {
        cs[i] = i+7;
        pinMode(cs[i], OUTPUT);

        //Command is the variable sent to DAC to drive pressure regulator
        //The command variable is comprised of the 4 configuration bits and 12 data
        //bits
        unsigned int command;
        //Shift the config bits 12 positions leftward, augment with the a[i] pressure
        //value
        //in volts
        command = ( Config << 12 | a[i] );

        //Write command to each ith DAQ
        SPI.beginTransaction(SPISettings(20000000, MSBFIRST, SPI_MODE0));
        //Set ith output pin to LOW, in order to accept write command
        digitalWrite(cs[i], LOW);
        //SPI.transfer function is only capable of sending 8bits at a time
        //The 16bit command is therefore split into a high and low byte
        int high = highByte(command);
        int low = lowByte(command);
    }
}
}

```

```

        SPI.transfer(high);
        SPI.transfer(low);
        SPI.endTransaction();
        //Set i'th pin HIGH to end write command
        digitalWrite(cs[i], HIGH);
        //Optional print for debugging
        //Serial.println("16bit command sent:");
        //Serial.println(value,BIN);
    }
}

//END DAC CODE

//START PRESSURE SENSOR CODE:

//Define buffer to hold sampled values
byte buffer[4];

for (int addr = 1; addr <= 8; addr++)
{
    //Pressure sensor addresses have been configured to 1 through 8.
    //Sensors 1,2,3,4 are high range 1000mbar
    if (addr <= 4)
    {
        //Set conversion constants for AMS 5915-1000-D
        p_min = 0;
        p_max = 1000;
        digoutp_min = 1638;
        digoutp_max = 14745;
    }

    //Sensors 5,6,7,8 are high resolution 350mbar
    else
    {
        //Set conversion constants for AMS 5915-350-D-B
        p_min = 0;
        p_max = 350;
        digoutp_min = 1638;
        digoutp_max = 14745;
    }

    //Wire.requestFrom(address, quantity)
    //address: the 7-bit address of the device to request bytes from
    //quantity: the number of bytes to request
    //request four bytes from sensor (first 2 are pressure, second 2 are temp)
    int n = Wire.requestFrom (addr, 4);

    //Ensure response is 4byte
    if(n == 4)
    {

        Wire.readBytes (buffer, 4);

        unsigned int p_raw = word (buffer[0], buffer[1]);      // word(high,low)
        unsigned int t_raw = word (buffer[2], buffer[3]);

        // note that the next bit operations works best with "unsigned int", not
        // with "int"
        p_raw &= 0x3FFF;      // 14bits pressure data
        t_raw >>= 5;          // 11bits temperature data, shift them in position

        // convert raw pressure to mbar (equation and constants from datasheet)
        float pressure = ((( (float) p_raw - digoutp_min ) / ((digoutp_max -
        digoutp_min) / (p_max - p_min))) + p_min );
    }
}

```

```

        // convert raw temperature to degC (equation and constants from datasheet
        )
        float temperature = (( (float) t_raw * 200.0 ) / 2048.0 ) - 50.0;

        // with the pressure comparison array with all sensor's outputs
        p_comp[addr-1] = pressure;
    }

//If no response is present, or response is not 4bytes
else
{
    Serial.println ("Error, no sensor found");
}
}

int i;
for (i = 0; i <= 3; i++)
{
    if (p_comp[i]> 350)
    {
        p_out[i] = p_comp[i];
    }
    else
    {
        p_out[i] = p_comp[i+4];
    }
    Serial.println(p_out[i]);
}
// END PRESSURE SENSOR CODE
}

```

Appendix B

LabVIEW VI

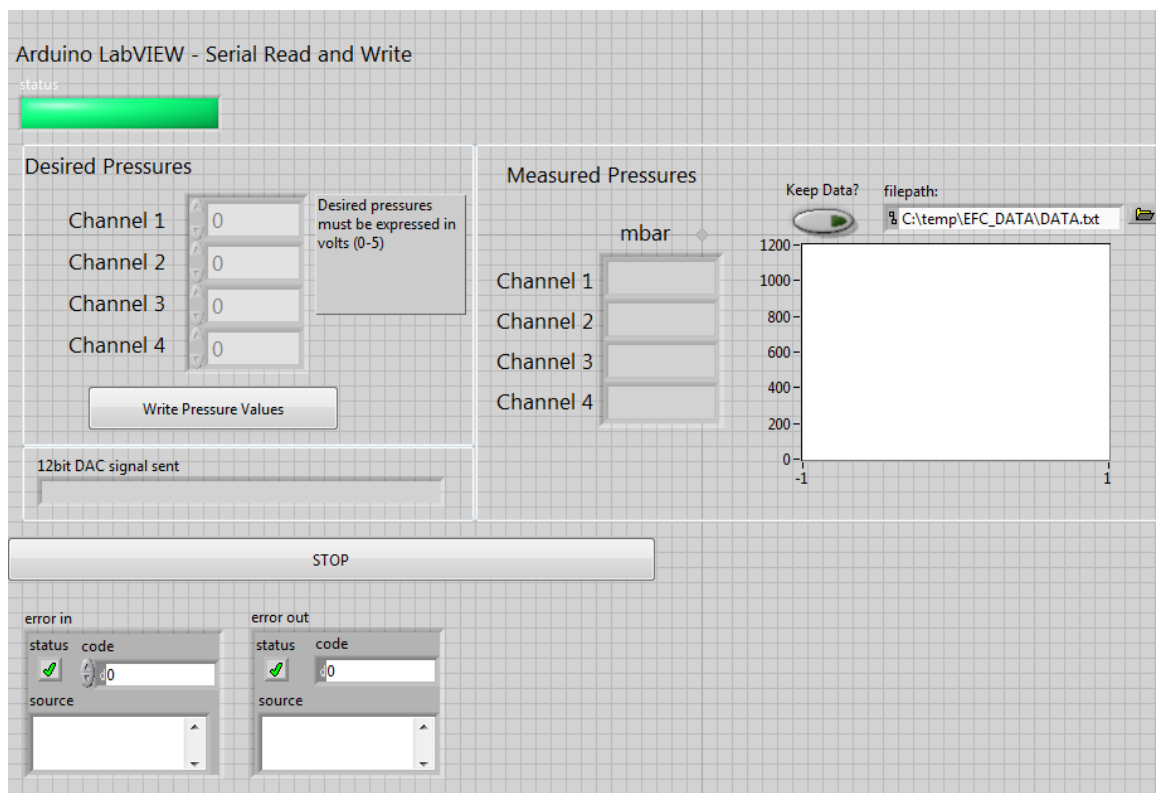


Figure B.1: LabVIEW Frontend

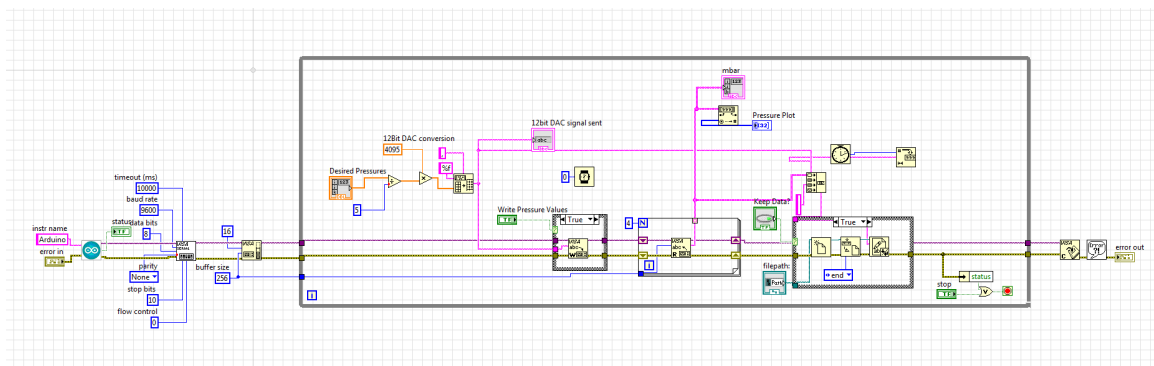
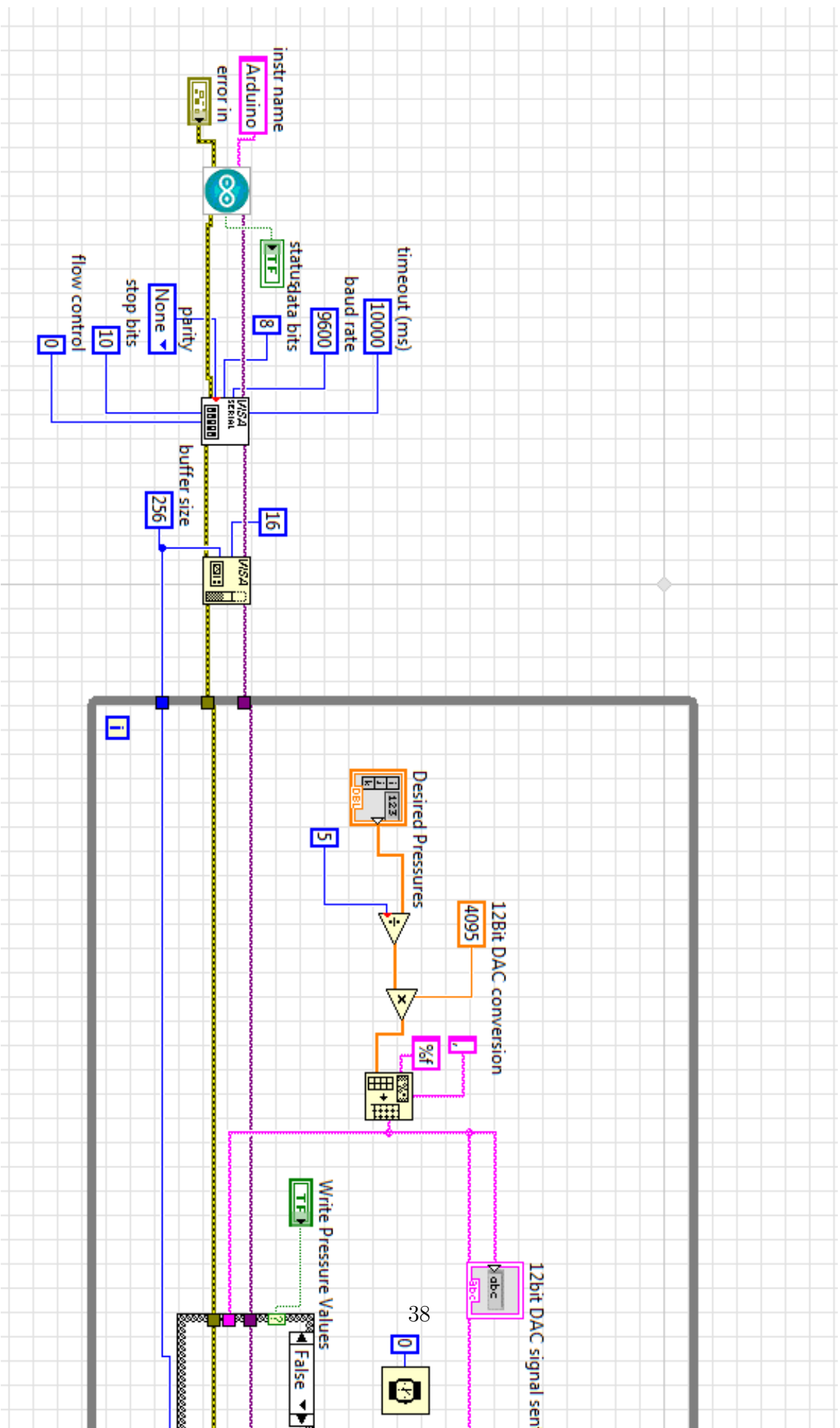


Figure B.2: LabVIEW Backend



Appendix C

Polydispersity Analysis

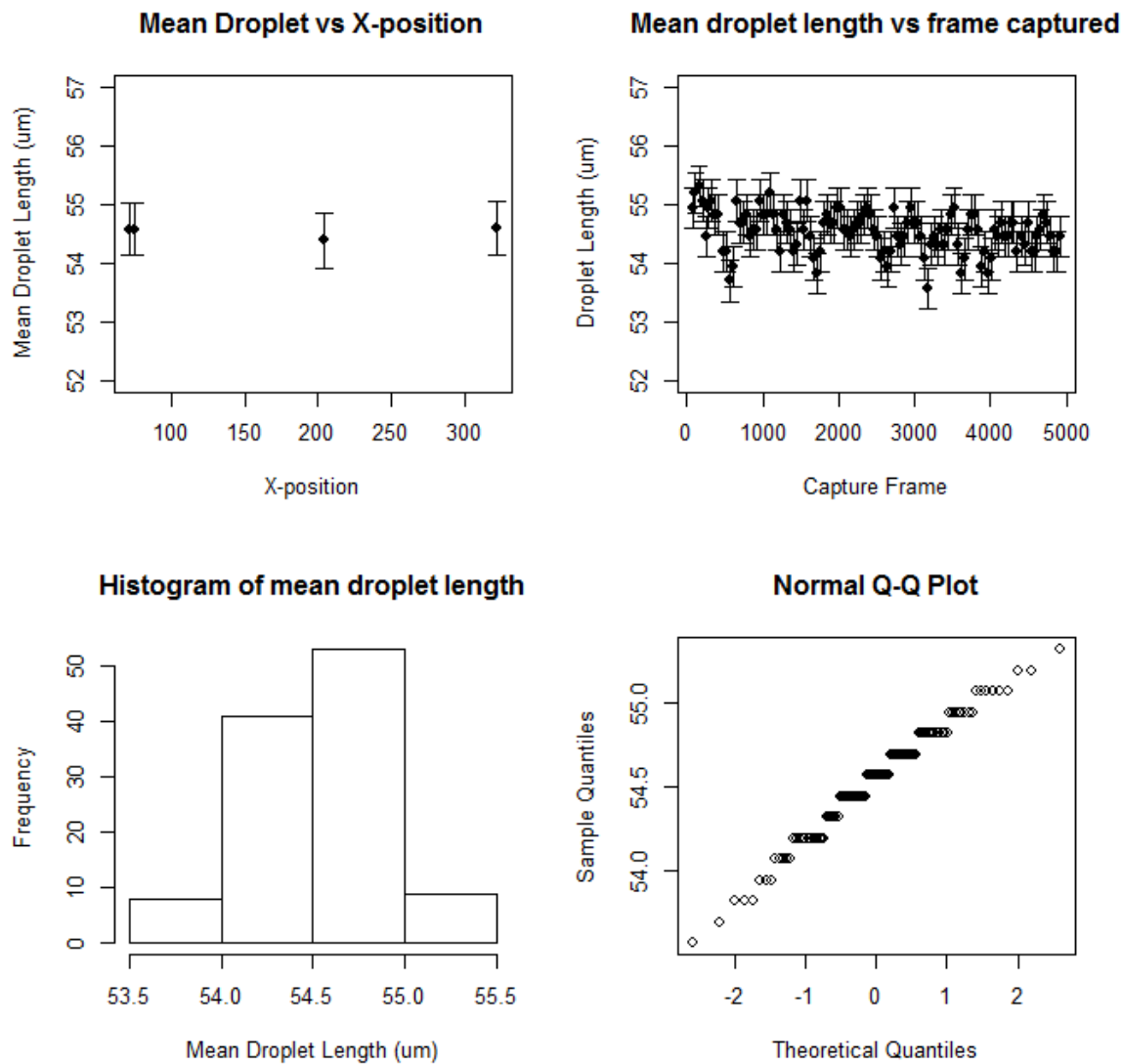


Figure C.1: Polydispersity at CA = 0.014

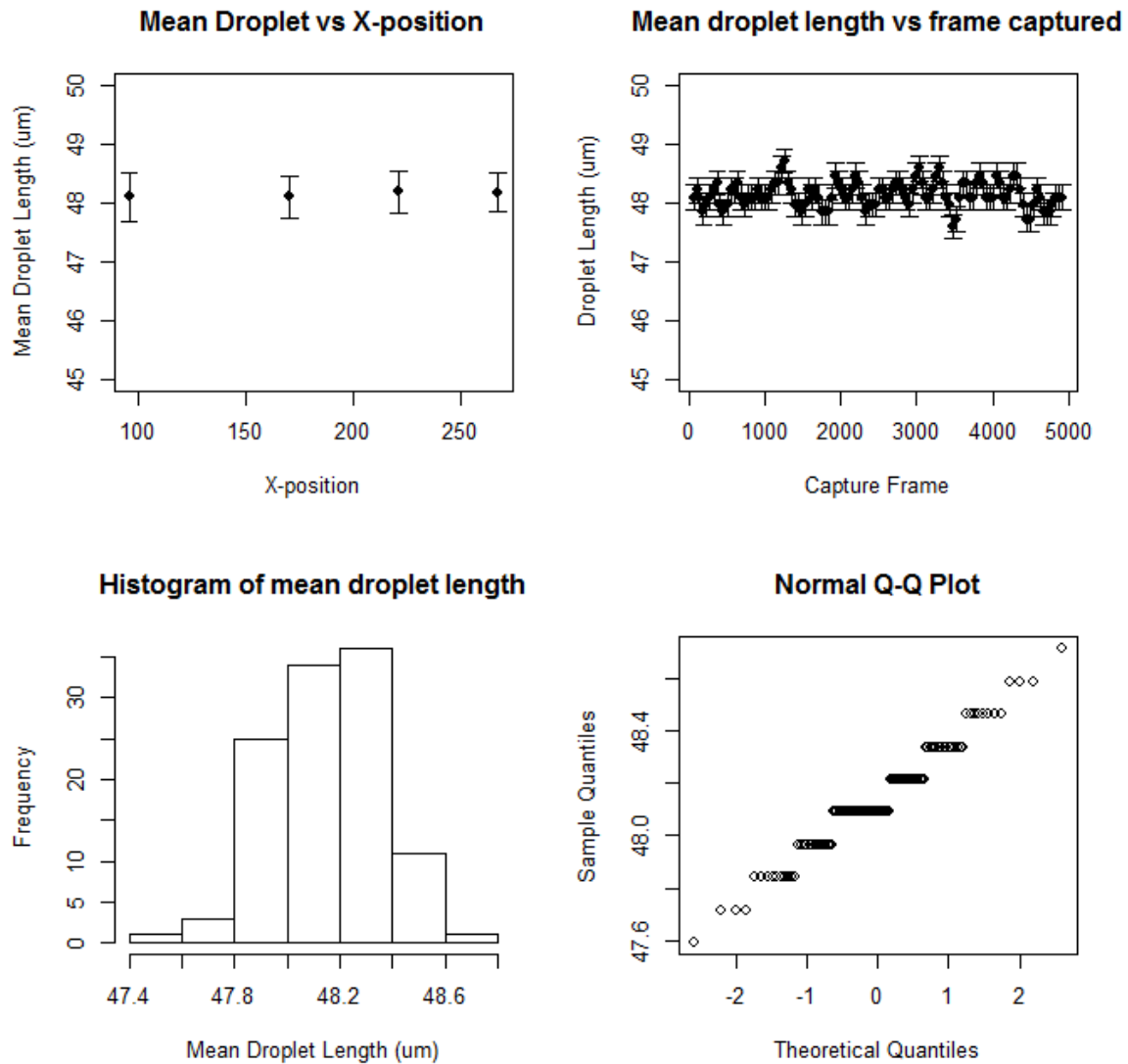


Figure C.2: Polydispersity at CA = 0.018

Bibliography

- [1] 3M. 3M Novec 7200 Engineered Fluid. Datasheet, 2009.
- [2] Adam R. Abate, Pascaline Mary, Volkert van Steijn, and David A. Weitz. Experimental validation of plugging during drop formation in a T-junction. *Lab on a Chip*, 12(8):1516, 2012.
- [3] Henrik Bruus. *Theoretical Microfluidics*. Oxford ; New York : Oxford University Press, 2008., 2008.
- [4] Lorenzo Capretto, Wei Cheng, Martyn Hill, and Xunli Zhang. Micromixing within microfluidic devices. *Topics in Current Chemistry*, 304(1):27–68, 2011.
- [5] Zhuang Zhi Chong, Say Hwa Tan, Alfonso M Ganan-Calvo, Shu Beng Tor, Ngiap Hiang Loh, and Nam-Trung Nguyen. Active droplet generation in microfluidics. *Lab Chip*, 16:35–58, 2016.
- [6] Gordon F. Christopher, N. Nadia Noharuddin, Joshua A. Taylor, and Shelley L. Anna. Experimental observations of the squeezing-to-dripping transition in T-shaped microfluidic junctions. *Physical Review E - Statistical, Nonlinear, and Soft Matter Physics*, 78(3), 2008.
- [7] Krzysztof Churski, Michal Nowacki, Piotr M. Korczyk, and Piotr Garstecki. Simple modular systems for generation of droplets on demand. *Lab on a Chip*, 13(18):3689–3697, 2013.
- [8] M. De Menech, P. Garstecki, F. Jousse, and H. a. Stone. Transition from squeezing to dripping in a microfluidic T-shaped junction. *Journal of Fluid Mechanics*, 595:141–161, 2008.
- [9] Piotr Garstecki, Michael J. Fuerstman, Howard A. Stone, and George M. Whitesides. Formation of droplets and bubbles in a microfluidic T-junctionscaling and mechanism of break-up. *Lab on a Chip*, 6(3):437, 2006.
- [10] Clement Kleinstreuer. *Microfluidics and Nanofluidics: Theory and Selected Applications: Theory and Selected Applications*. 2013.
- [11] Zida Li, Sze Yi Mak, Alban Sauret, and Ho Cheung Shum. Syringe-pump-induced fluctuation in all-aqueous microfluidic system implications for flow rate accuracy. *Lab on a Chip*, 14(4):744, 2014.
- [12] Princeton Microfluidics. Microfluidics Bootcamp 2014. 2014.
- [13] Lothar Schmid and Thomas Franke. Acoustic modulation of droplet size in a T-junction. *Applied Physics Letters*, 104(13):133501 p.1–4, 2014.
- [14] Lingling Shui, J. C T Eijkel, and Albert van den Berg. Multiphase flow in micro- and nanochannels. *Sensors and Actuators, B: Chemical*, 121(1):263–276, 2007.
- [15] Lingling Shui, Jan C T Eijkel, and Albert van den Berg. Multiphase flow in microfluidic systems - Control and applications of droplets and interfaces. *Advances in Colloid and Interface Science*, 133(1):35–49, 2007.
- [16] H A Stone, A D Stroock, and A Ajdari. ENGINEERING FLOWS IN SMALL DEVICESMicrofluidics Toward a Lab-on-a-Chip. *Annual Review of Fluid Mechanics*, 36(1):381–411, 2004.
- [17] A.D. Stroock and G.M. Whitesides. Components for integrated poly (dimethylsiloxane) microfluidic systems. *Electrophoresis*, 23(20):3461–3473, 2002.
- [18] Thomas Ward, Magalie Faivre, Manouk Abkarian, and Howard A. Stone. Microfluidic flow focusing: Drop size and scaling in pressure versus flow-rate-driven pumping. *Electrophoresis*, 26(19):3716–3724, 2005.
- [19] Chun Guang Yang, Zhang Run Xu, and Jian Hua Wang. Manipulation of droplets in microfluidic systems. *TrAC - Trends in Analytical Chemistry*, 29(2):141–157, 2010.

- [20] Chun Xia Zhao and Anton P J Middelberg. Two-phase microfluidic flows. *Chemical Engineering Science*, 66(7):1394–1411, 2011.